Particle-Particle Random Phase Approximation for Predicting Correlated Excited States of Point Defects

Jiachen Li,[*,†] Yu Jin,[‡] Jincheng Yu,[¶] Weitao Yang,[*,¶] and Tianyu Zhu[*,†]

†*Department of Chemistry, Yale University, New Haven, Connecticut 06520, United States*

‡*Pritzker School of Molecular Engineering, University of Chicago, Chicago, Illinois 60637, United States*

¶*Department of Chemistry, Duke University, Durham, North Carolina 27708, United States*

E-mail: jiachen.li@yale.edu; weitao.yang@duke.edu; tianyu.zhu@yale.edu

Abstract

The particle-particle random phase approximation (ppRPA) within the hole-hole channel was recently proposed as an efficient tool for computing excitation energies of point defects in solids [*J. Phys. Chem. Lett.* 2024, 15, 2757-2764]. In this work, we investigate the application of ppRPA within the particle-particle channel for predicting correlated excited states of point defects, including the carbon-vacancy (VC) in diamond, the oxygen-vacancy (VO) in magnesium oxide (MgO), and the carbon dimer defect (C_BC_N) in two-dimensional hexagonal boron nitride (h-BN). Starting from a density functional theory calculation of the $(N-2)$-electron ground state, vertical excitation energies of the N-electron system are obtained as the differences between the two-electron addition energies. We show that active-space ppRPA with the B3LYP functional yields accurate excitation energies, with errors mostly smaller than 0.1 eV

for tested systems compared to available experimental values. We further develop a natural transition orbital scheme within ppRPA, which provides insights into the multireference character of defect states. This study, together with our previous work, establishes ppRPA as a low-cost and accurate method for investigating excited-state properties of point defect systems.

1 INTRODUCTION

Optically active point defects in semiconductors and insulators are promising platforms for quantum information processing due to their special optical and magnetic properties.[1,2] In many point defect systems, defect energy levels are introduced within the fundamental gap of the host material, and the transitions among them can absorb or emit photons at lower energies than the optical gap of the pristine host material. The properties of the pristine host material are thus significantly changed, offering distinct advantages in applications of quantum information science.[3–5] These point defects may function as quantum bits (qubits), and the qubit initialization and readout are enabled by an optical spin-polarization cycle involving both radiative and spin-selective non-radiative transitions between many-body ground and excited states.[6,7] To assist in the interpretation of experiment results and gain deeper insights into materials design, theoretical simulations play an important role in the identification and characterization of point defects.

In past decades, many efforts have been devoted to developing theoretical approaches for the accurate description of excited states of point defect systems. Because of the good balance between the computational cost and accuracy, density functional theory (DFT)[8–10] based methods have been widely used to study point defects. Linear-response time-dependent density functional theory (TDDFT)[11,12] and ΔSCF[13–16] have been the most popular tools for calculating excited-state properties of point defects, such as excitation energies, geometry relaxations of excited states, and optical absorption and emission spectra.[17,18] However, it is challenging for methods based on a single Kohn-Sham (KS) determinant to describe

defect states with strong multireference characters.[19–21] To obtain more reliable treatments of the correlated excited states, quantum many-body methods including the Bethe-Salpeter equation approach within the Green's function formalism (i.e., GW-BSE),[22–24] equation-of-motion coupled-cluster theory,[25] and quantum Monte Carlo[26] have been applied. Nevertheless, their further applications to large point defect systems are limited either by their high computational costs or inherent single-reference nature. Recently, many flavors of quantum embedding approaches have been developed to describe correlated defect systems with affordable computational costs. The quantum embedding formalism provides a natural way to focus computation on a chosen active space representing the localized defect states with accurate but computationally demanding high-level theories, while the remaining environment is treated by efficient low-level theories.[27–32] It has been shown that the quantum defect embedding theory (QDET),[33–35] the density matrix embedding theory (DMET),[36–38] the constrained random phase approximation (cRPA) combined with exact diagonalization (ED),[39,40] the dynamical downfolding approach,[41] and the regional embedding theory[42] have achieved mixed successes in simulating point defect systems.

Parallel to particle-hole formalisms such as TDDFT and BSE, the particle-particle random phase approximation (ppRPA)[43,44] offers another path to compute excitation energies from the particle-particle and hole-hole channels. ppRPA that is originally developed for treating nuclear many-body interactions[45,46] has been formulated to describe various properties of molecular systems.[43,44] Compared with particle-hole random phase approximation (phRPA) that describes the response of the density matrix to an external perturbation, ppRPA describes the response of the pairing matrix to a perturbation in the form of a pairing field, which leads to two-electron addition and removal energies.[43,44] Therefore, the neutral excitation energy of an N-electron system can be obtained from the energy difference between two-electron addition energies of the corresponding $(N-2)$-electron system, or the energy difference between two-electron removal energies of the corresponding $(N+2)$-electron system. It has been shown that ppRPA provides good accuracy for modeling excited-state

properties of molecular systems such as excitation energies,[47–59] oscillator strengths,[48] conical intersection,[60] and potential energy surfaces.[61] Along with excited-state properties, ppRPA can also be used to calculate ground-state properties such as total energies and geometries.[43,44,47,53,56,61] For ground states, the ppRPA correlation energy is shown to be equivalent to the ladder-coupled-cluster doubles.[62,63] Excitation energies obtained from ppRPA can be considered as an approximation to double-electron-affinity or double-ionization-potential equation-of-motion coupled-cluster doubles.[48,64] In the context of DFT, ppRPA is the first known functional that captures the energy derivative discontinuity in strongly correlated systems and has no delocalization error in single-bond dissociations.[43,44] In the Green's function formalism, ppRPA eigenvalues and eigenvectors are used to construct the T-matrix self-energy for predicting quasiparticle energies[65–68] and the BSE kernel for neutral excitation energies.[69–71]

Recently, we employed ppRPA to calculate vertical excitation energies (VEEs) of point defects,[72] which is the first application of ppRPA to realistic periodic bulk systems. In Ref. 72, VEEs of point defects are computed from the hole-hole channel in ppRPA, which is the difference between the lowest and a higher two-electron removal energy of the $(N+2)$-electron ground state. It shows that ppRPA predicts accurate VEEs of the nitrogen-vacancy (NV^-) and the silicon-vacancy (SiV^0) centers in diamond and the divacancy center (VV^0) in 4H silicon carbide with errors smaller than 0.2 eV when using the B3LYP functional.[73,74] For these point defects, the corresponding $(N+2)$-electron systems are closed-shell, and all desired defect excited states can be accessed by removing two electrons. Besides excellent accuracy, ppRPA is computationally favorable and cheaper than the corresponding ground-state DFT calculation by combining with the recently developed active-space approach.[68] The ppRPA excitation energies calculated from the hole-hole channel demonstrate rapid convergence, requiring just a few hundred canonical orbitals in the active space, which is independent of the specific defect system.[72]

In this work, we further establish the applicability of ppRPA in predicting correlated

excited states of point defects by investigating two important extensions. First, the particle-particle channel in ppRPA is adopted to calculate VEEs of point defect systems, including the carbon-vacancy (VC) in diamond, the oxygen-vacancy (VO) in magnesium oxide (MgO), and the carbon dimer (C_BC_N) defect in two-dimensional hexagonal boron nitride (h-BN). Compared with previous work that starts with the $(N+2)$-electron ground state,[72] this work employs the $(N-2)$-electron ground state computed at the DFT level as the reference in ppRPA calculations. By removing two electrons from the original N-electron defect system, the $(N-2)$-electron ground state becomes closed-shell for systems studied in this paper, which can be properly described by single-determinant KS-DFT. All desired excitation energies can then be obtained by taking the differences between two-electron addition energies of the $(N-2)$-electron system. To reduce the computational cost, the ppRPA equation is solved with the Davidson algorithm[49] in the canonical active space,[68] then excitation energies at the full-system limit are obtained by an active-space extrapolation scheme. We demonstrate that ppRPA predicts accurate excitation energies for all tested defect systems. Second, we develop a natural transition orbital (NTO) approach within ppRPA to gain further insights into the character of defect excited states. In analogy to NTOs in particle-hole methods such as TDDFT and BSE,[75–77] NTOs in ppRPA are obtained from the singular value decomposition (SVD) of ppRPA eigenvectors. Similar to other local orbital approaches that provide the understanding of chemical reactivity,[78–83] NTOs in ppRPA provide a compact orbital representation for two-electron addition and removal processes. The weights of NTOs are used to qualitatively measure the multireference character of defect states.

The remainder of this article is organized as follows. We review the ppRPA formalism and introduce the NTO approach in ppRPA in Section 2. The computational details about our calculations are given in Section 3. The active-space extrapolation scheme, predicted VEEs of tested point defects, and the NTO analysis for the multireference character of defect states are presented in Section 4. We finally draw conclusions in Section 5.

2 THEORY

2.1 Excitation Energy from ppRPA

We first review the ppRPA formalism. ppRPA can be derived from different approaches, including the equation of motion,[45,84] the adiabatic connection,[43,44] and TDDFT with the pairing field.[85] As the counterpart of phRPA, ppRPA describes the instantaneous fluctuation of the pairing matrix[43,44]

$$\kappa(x_1, x_2) = \langle \Psi_0^N | \hat{\psi}(x_2) \hat{\psi}(x_1) | \Psi_0^N \rangle \tag{1}$$

The pairing matrix κ is zero for a system with a fixed number of electrons and has non-vanished fluctuations to a perturbation in the form of a pairing field.[43] Here, $x = (r, \sigma)$ is the space-spin combined variable, Ψ_0^N is the N-electron ground state, $\hat{\psi}^\dagger$ and $\hat{\psi}$ are creation and annihilation operators in the second-quantization notation. In the linear-response theory, the paring matrix $\delta\kappa(x_1, x_2)$ is non-zero when the system is perturbed by an external field in the form of a pairing field.[43] In the frequency domain, the time-ordered pairing matrix fluctuation that describes the linear response of the pairing matrix is[43,44]

$$K_{pqrs}(\omega) = \sum_m \frac{\langle \Psi_0^N | \hat{a}_p \hat{a}_q | \Psi_m^{N+2} \rangle \langle \Psi_m^{N+2} | \hat{a}_s^\dagger \hat{a}_r^\dagger | \Psi_0^N \rangle}{\omega - \Omega_m^{N+2} + i\eta} - \sum_m \frac{\langle \Psi_0^N | \hat{a}_s^\dagger \hat{a}_r^\dagger | \Psi_m^{N-2} \rangle \langle \Psi_m^{N-2} | \hat{a}_p \hat{a}_q | \Psi_0^N \rangle}{\omega - \Omega_m^{N-2} - i\eta} \tag{2}$$

where $\hat{a}_p^\dagger$ and $\hat{a}_p$ are creation and annihilation operators in the second-quantization notation, $\Omega^{N\pm2}$ is the two-electron addition/removal energy, and η is a positive infinitesimal number. In Eq. 2 and the following, we use i, j, k, l for occupied orbitals, a, b, c, d for virtual orbitals, p, q, r, s for general molecular orbitals, and m for the index of the two-electron addition/removal energy. In ppRPA, K is approximated in terms of the non-interacting K^0 via the Dyson equation[43,44]

$$K = K^0 + K^0 V K \tag{3}$$

where the antisymmetric interaction is $V_{pq,rs} = \langle pq||rs\rangle = \langle pq|rs\rangle - \langle pq|sr\rangle$ with $\langle pq|rs\rangle = \int d\mathbf{x}d\mathbf{x}' \frac{\psi_p^*(\mathbf{x})\psi_r(\mathbf{x})\psi_q^*(\mathbf{x}')\psi_s(\mathbf{x}')}{|\mathbf{r}-\mathbf{r}'|}$.

Eq. 3 can be cast into a generalized eigenvalue problem that gives two-electron addition and removal energies[43,49]

$$\begin{bmatrix} \mathbf{A} & \mathbf{B} \\ \mathbf{B}^{\mathrm{T}} & \mathbf{C} \end{bmatrix} \begin{bmatrix} \mathbf{X} \\ \mathbf{Y} \end{bmatrix} = \Omega \begin{bmatrix} \mathbf{I} & \mathbf{0} \\ \mathbf{0} & -\mathbf{I} \end{bmatrix} \begin{bmatrix} \mathbf{X} \\ \mathbf{Y} \end{bmatrix} \tag{4}$$

with

$$A_{ab,cd} = \delta_{ac}\delta_{bd}(\epsilon_a + \epsilon_b) + \langle ab||cd\rangle \tag{5}$$

$$B_{ab,kl} = \langle ab||kl\rangle \tag{6}$$

$$C_{ij,kl} = -\delta_{ik}\delta_{jl}(\epsilon_i + \epsilon_j) + \langle ij||kl\rangle \tag{7}$$

where $a < b$, $c < d$, $i < j$, $k < l$, Ω is the two-electron addition/removal energy, X and Y are the two-electron addition and removal eigenvectors. The ppRPA eigenvector is normalized as[43,44]

$$X^{m,\dagger}X^m - Y^{m,\dagger}Y^m = \pm 1 \tag{8}$$

where the upper sign is for two-electron addition excitations and the lower sign is for two-electron removal excitations.

In this work, to obtain the neutral excitation energies of the N-electron system, we first perform the self-consistent field (SCF) calculation of the $(N-2)$-electron system, then calculate excitation energies as the differences between the lowest and a higher two-electron addition energies from Eq. 4. The neutral excitation energies of the N-electron system can also be obtained as the differences between the lowest and a higher two-electron removal energies of the $(N+2)$-electron system, which has been used previously for predicting excitation energies of molecules and point defects.[57–59,72]

For the studied point defects in this work, the corresponding $(N-2)$-electron systems are closed-shell and can be calculated with spin-restricted DFT, which is cheaper than spin-unrestricted DFT/HF typically used in TDDFT and quantum embedding approaches and is free of spin contamination. For closed-shell systems, the ppRPA equation in Eq. 4 can be cast into the spin-adapted equation,[47] where for triplet excitations, the ppRPA matrix elements are

$$A^{\mathrm{t}}_{ab,cd} = \delta_{ac}\delta_{bd}(\epsilon_a + \epsilon_b) + \langle ab||cd\rangle \tag{9}$$

$$B^{\mathrm{t}}_{ab,kl} = \langle ab||kl\rangle \tag{10}$$

$$C^{\mathrm{t}}_{ij,kl} = -\delta_{ik}\delta_{jl}(\epsilon_i + \epsilon_j) + \langle ij||kl\rangle \tag{11}$$

with $a < b$, $c < d$, $i < j$ and $k < l$, and for singlet excitations the ppRPA matrix elements are

$$A^{\mathrm{s}}_{ab,cd} = \delta_{ac}\delta_{bd}(\epsilon_a + \epsilon_b) + \frac{1}{\sqrt{(1+\delta_{ab})(1+\delta_{cd})}}(\langle ab|cd\rangle + \langle ab|dc\rangle) \tag{12}$$

$$B^{\mathrm{s}}_{ab,kl} = \frac{1}{\sqrt{(1+\delta_{ab})(1+\delta_{kl})}}(\langle ab|kl\rangle + \langle ab|lk\rangle) \tag{13}$$

$$C^{\mathrm{s}}_{ij,kl} = -\delta_{ik}\delta_{jl}(\epsilon_i + \epsilon_j) + \frac{1}{\sqrt{(1+\delta_{ij})(1+\delta_{kl})}}(\langle ij|kl\rangle + \langle ij|lk\rangle) \tag{14}$$

with $a \leq b$, $c \leq d$, $i \leq j$ and $k \leq l$.

For point defects whose corresponding $(N-2)$-electron system face convergence difficulties in SCF calculations, KS orbitals and orbital energies obtained from the N-electron system are used in Eq. 4, which is denoted as ppRPA*.[48] In ppRPA*, the reference is a non-optimized single determinant for the $(N-2)$-electron system, similar in spirit to spin-flip methods. ppRPA* has been applied to predict valence, Rydberg, and double excitation energies for small molecules,[48] and we will investigate its reliability for defect systems here.

The ppRPA working equation defined in Eq. 4 has a similar structure as the Casida equation in TDDFT,[11,12] which can be solved with the Davidson algorithm with the $\mathcal{O}(N^4)$

scaling (N is the number of orbitals in the system).[49] In this work, the Davidson algorithm is combined with the active space approach developed in Ref. 68 to lower the cost of ppRPA calculations. The full-space results are obtained through an extrapolation scheme using data from a series of different active-space calculations.

2.2 Natural Transition Orbital in ppRPA

To analyze the character of defect excited states, we further develop the NTO approach within ppRPA. The NTO concept has been widely used in particle-hole formalisms such as TDDFT and BSE to provide qualitative descriptions of electronic transitions.[75,77] In the NTO approach of particle-hole formalisms, the dominant particle-hole pair in the excited state is obtained by the SVD of the corresponding transition density matrix.[75]

Parallel to NTOs in the particle-hole formalisms that describe particle-hole transitions, NTOs in ppRPA convey information about particle-particle pairs and hole-hole pairs. For the m-th state, the two-electron addition eigenvector X^m can be viewed as a triangular matrix with of dimension $N_{\text{vir}} \times N_{\text{vir}}$ and the two-electron removal eigenvector Y^m can be viewed as a triangular matrix with of dimension $N_{\text{occ}} \times N_{\text{occ}}$. Thus, coefficients from molecular orbitals to natural transition orbitals of two particles (holes) can be obtained with the SVD of X^m (Y^m)

$$X^m = C^{\text{p1},m} \sqrt{\lambda^{\text{p},m}} C^{\text{p2},m\dagger} \tag{15}$$

$$Y^m = C^{\text{h1},m} \sqrt{\lambda^{\text{h},m}} C^{\text{h2},m\dagger} \tag{16}$$

In Eq. 15, the NTO coefficient matrices C^{p1} and C^{p2} of dimension $N_{\text{vir}} \times N_{\text{vir}}$ are associated with particle-particle pairs for adding the first and second electrons, which are weighted with diagonal elements of matrix λ^{p}. Similarly, in Eq. 16, the NTO coefficient matrices C^{h1} and C^{h2} of dimension $N_{\text{occ}} \times N_{\text{occ}}$ are associated with hole-hole pairs for removing the first and second electrons, which are weighted with diagonal elements of matrix λ^{h}. As a consequence

of the normalization in Eq. 8, the NTO weights satisfy the following relation

$$\sum_{a}^{\text{vir}} \lambda_a^{\text{p}} - \sum_{i}^{\text{occ}} \lambda_i^{\text{h}} = \pm 1 \tag{17}$$

where the upper sign is for two-electron addition excitations and the lower sign is for two-electron removal excitations. The resulting NTO weights (λ_a^{p} and λ_i^{h}) can thus be employed to qualitatively analyze the components and multireference character of the associated ground and excited states.

3 COMPUTATIONAL DETAILS

Ground-state geometries of all three defect systems were optimized with the PBE functional[86] using the Quantum ESPRESSO package,[87,88] and details can be found in the Supporting Information (SI). We then performed $(N-2)$-electron ground-state DFT calculations for VC in diamond and VO in MgO. For C_BC_N in two-dimensional h-BN, due to the convergence difficulty in the $(N-2)$-electron ground-state DFT calculation, the N-electron ground-state DFT calculation was performed. All ground-state DFT calculations in periodic Gaussian basis sets were carried out using the PySCF quantum chemistry software package[89,90] with Γ-point sampling and Gaussian density fitting. Two functionals (PBE[86] and B3LYP[73,74]) were used in combination with the cc-pVDZ basis set[91] and the corresponding cc-pVDZ-RI auxiliary basis set.[92] With electron integrals and DFT solutions obtained from PySCF, we further performed active-space ppRPA calculations with periodic boundary condition to predict VEEs of point defects using the `Lib_ppRPA` library.[93] The low-lying excited states are highly localized within defect levels and can thus be well described by DZ-level basis sets. As shown in the SI, using the cc-pVTZ basis set leads to very close VEE results as those obtained with the cc-pVDZ basis set, so we only present results computed using the cc-pVDZ basis. This convergence behavior with respect to basis sets is similar to excitation energies obtain from the hole-hole channel shown in our previous work.[72]

4 RESULTS

4.1 Extrapolation of Active-Space Results to Full-Space Limit

We first establish the extrapolation scheme to obtain the full-space results in the active-space ppRPA approach. The VEEs of VC in diamond with D_{2d} symmetry and VO in MgO obtained from ppRPA@B3LYP using supercell models containing 215 atoms are shown in Fig. 1. The supercell of VC in diamond has 644 occupied and 2366 virtual orbitals, while the supercell of VO in MgO has 1075 occupied and 2043 virtual orbitals. As shown in Eq. 5, the **A** matrix in ppRPA has four indexes of virtual orbitals, so an active-space approach is desired to reduce the computational cost in the calculations of large supercell models. For simplicity, the active spaces used in this work include the same numbers of occupied and virtual canonical molecular orbitals around the Fermi level, which are consistent with Refs. 68 and 72. As shown in Fig. 1, similar convergence patterns are observed for both point defect systems. We find a linear relationship between the excitation energies and the inverse of the number of active-space orbitals (denoted as N_{orb}). The excitation energy at the full-space limit is thus obtained from the extrapolation of active-space values against $1/N_{\text{orb}}$, similar to schemes adopted in the quantum embedding literature.[37,42] In this work, we use the active spaces containing 400, 500, 600, and 800 orbitals in the four-point extrapolation scheme to obtain the full-space results.

Compared with previous works for molecular[68] and point defect systems,[72] the convergence of active-space ppRPA results is slower in this study for two reasons. First, the number of orbitals needed in the active space for periodic systems is larger due to the denser manifold of low-lying states in solids than in molecules. Second, the convergence of two-electron addition energies from the particle-particle channel mainly depends on the virtual space, which is more difficult to converge than the occupied space in the hole-hole channel.[72] Nevertheless, the size of the active space needed for reliable extrapolation is still much smaller than the size of the full space. We note, in principle, natural orbitals from diagonalizing the density

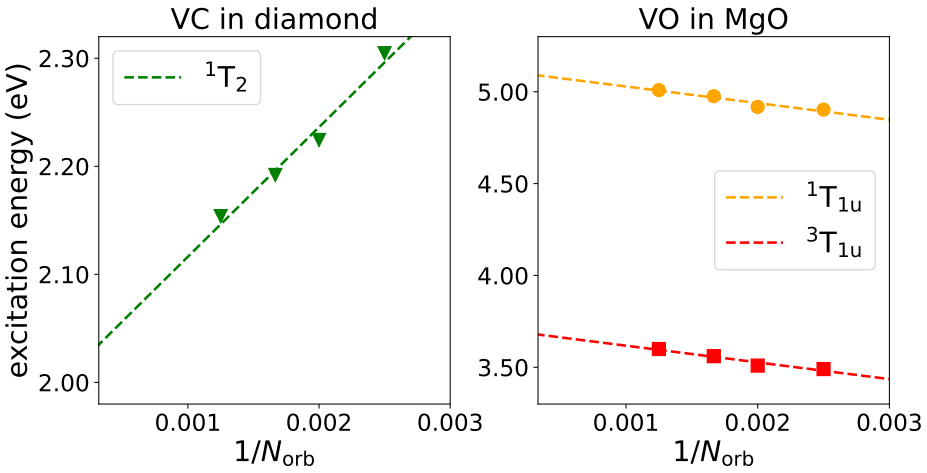

Figure 1: Extrapolations of VEEs with respect to the inverse of the active-space size. N_{orb} is the number of canonical orbitals in the active space, and the cc-pVDZ basis set was used. Left: $^1\mathrm{T}_2$ state of VC in diamond with $\mathrm{D}_{2\mathrm{d}}$ symmetry (215-atom supercell). Right: $^1\mathrm{T}_{1\mathrm{u}}$ and $^3\mathrm{T}_{1\mathrm{u}}$ states of VO in MgO (215-atom supercell).

matrix of a correlated or excited-state method can be used to construct the active space and further reduce the computational cost.

4.2 Vertical Excitation Energies

4.2.1 VC in diamond

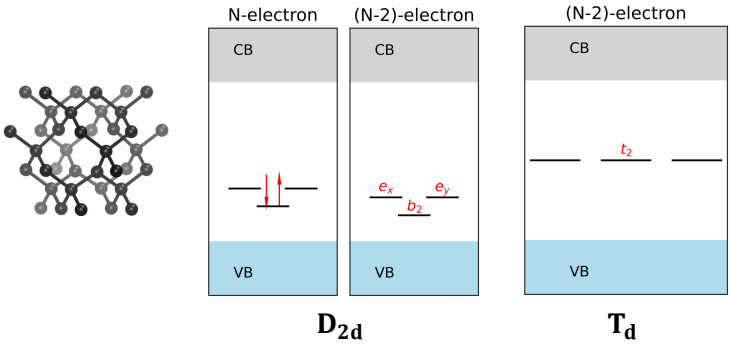

Figure 2: Illustration of defect energy levels and ground-state electron configurations of VC in diamond with $\mathrm{D}_{2\mathrm{d}}$ and T_{d} symmetries (energy levels are qualitative only). The electron configuration of N-electron state with T_{d} symmetry is not shown because it is a multiconfigurational state.

Our first tested system is VC in diamond. The predicted VEEs of its excited state from

Table 1: VEEs of VC in diamond obtained from the ppRPA approach based on PBE and B3LYP functionals compared with reference values. Supercell-size extrapolated values were obtained from the results of supercells containing 63 and 215 atoms. The geometry with D_{2d} or T_d symmetry was employed, where the corresponding excited state is ^1E (D_{2d}) or $^1T_2$ (T_d) state. The cc-pVDZ basis set was used. All values are in eV.

Method	Structure	$^1E/^1T_2$
Experiment[94]		2.2
ppRPA@PBE (supercell 215)	D_{2d}	1.67
ppRPA@PBE (extrapolated)	D_{2d}	1.77
ppRPA@B3LYP (supercell 215)	D_{2d}	2.02
ppRPA@B3LYP (extrapolated)	D_{2d}	2.15
ppRPA@PBE (supercell 215)	T_d	1.51
ppRPA@PBE (extrapolated)	T_d	1.56
ppRPA@B3LYP (supercell 215)	T_d	1.81
ppRPA@B3LYP (extrapolated)	T_d	1.89
TDDFT@PBE (supercell 215)	D_{2d}	1.19
TDDFT@PBE (extrapolated)	D_{2d}	1.26
TDDFT@B3LYP (supercell 215)	D_{2d}	1.30
TDDFT@B3LYP (extrapolated)	D_{2d}	1.40
CCSD[42]	D_{2d}	2.09
DMC[95]	T_d	1.51±0.34
ΔSCF@B3LYP[16]	T_d	1.57

the ppRPA approach based on PBE and B3LYP are presented in Table 1. To correct the finite supercell-size error, we also employed a two-point supercell-size extrapolation scheme, using 63-atom and 215-atom excitation energies in a linear fitting of the form: $E(1/N_{\text{atom}}) = E_\infty + a/N_{\text{atom}}$, which has been successfully used to predict VEEs of defect systems in the thermodynamic limit.[17,38,72] Ground-state geometries of both D_{2d} and T_d symmetries were used in ppRPA calculations. In the calculations with the D_{2d} geometry, the symmetry of the studied defect excited state is ^1E, while the defect excited state is $^1T_2$ in the T_d geometry.

As shown in Fig. 2, in the statically distorted D_{2d} geometry, the lowest defect orbital (b_2) is doubly occupied and the unoccupied defect orbitals (e_x and e_y) are two-fold degenerate. In the corresponding $(N-2)$-electron state, two electrons are removed from the lowest defect

orbital (b_2). Thus, both N-electron and $(N-2)$-electron ground states may be described by a single determinant. Although the N-electron ground state is a closed-shell singlet, TDDFT based on both GGA and hybrid functionals (i.e., PBE and B3LYP) has large errors around or larger than 0.8 eV for predicting the VEE. This large error can be attributed to the insufficient description of the ground state using a single KS determinant. As will be seen in Section 4.3, the ppRPA@B3LYP NTO analysis shows that the singlet ground state in the D_{2d} geometry consists of $\sim 87\%$ contribution from the $|b_2\bar{b}_2\rangle$ configuration, while the remaining $\sim 13\%$ contribution comes from the doubly-excited configurations $|e_x\bar{e}_x\rangle$ and $|e_y\bar{e}_y\rangle$. Single-determinant TDDFT starts with a pure $|b_2\bar{b}_2\rangle$ configuration, which is responsible for its limited accuracy. In ppRPA, these two defect-level electrons are treated in a subspace configuration interaction (CI) fashion, so near-degenerate configurations can be treated on equal footing. ppRPA based on PBE underestimates the VEE by more than 0.4 eV, which agrees with our previous results for other defect systems,[72] although it is already substantially better than TDDFT. The extrapolated ppRPA@B3LYP provides further improved accuracy. It predicts accurate VEE with an error smaller than 0.1 eV, which is comparable to more expensive EOM-CCSD (equation-of-motion coupled-cluster singles and doubles).[42]

Next, we turn to the results based on the T_d geometry, which is consistent with the tetrahedral symmetry observed in the experiment[94] (although the D_{2d} geometry may also be relevant through a dynamic Jahn-Teller mechanism[94,96,97]). As shown in Fig. 2, orbitals with t_2 symmetry are threefold degenerate. For the N-electron system, two electrons are filled into three degenerate orbitals, indicating that the ground state has a strong multiconfigurational character. As a result, single-reference approaches are not appropriate here. By removing two electrons, the ground state of the $(N-2)$-electron system used in ppRPA is a well-behaved closed-shell singlet state without dramatic static correlation, which can be well described by DFT. Therefore, ppRPA does not suffer from large static correlation error and predicts accurate VEEs. To directly compare with the literature values, the VEE of the $^1T_2$ state is obtained as the difference between two-electron addition energies of $^1T_2$

excited and ^{1}E ground state. As shown in Table 1, both ppRPA@PBE and ppRPA@B3LYP provide reasonably accurate results; for example, ppRPA@B3LYP only underestimates the VEE by 0.3 eV. This performance is more accurate than ΔSCF and even slightly better than the more costly diffusion quantum Monte Carlo (DMC). Through a seamless combination of DFT for the $(N-2)$-electron system and a subspace CI for the two valence electrons, ppRPA provides a balanced description of the challenging ground and excited states in the T_d geometry with a low cost. We note that, the slightly larger errors in ppRPA predictions for the T_d geometry may result from less accurate DFT geometry optimization, where each of the three degenerate t_2 KS orbitals was enforced to accommodate 2/3 of an electron.

4.2.2 VO in MgO

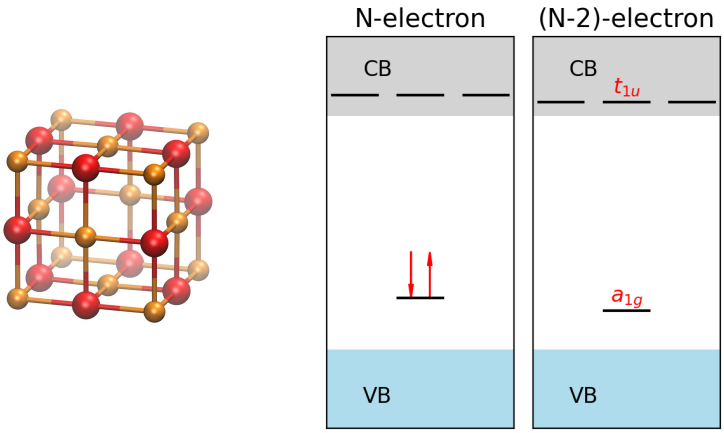

Figure 3: Illustration of defect energy levels and ground-state electron configurations of VO in MgO (energy levels are qualitative only).

We now turn to the discussion of VO in MgO. The VEEs of the $^1T_{1u}$ and $^3T_{1u}$ states of VO in MgO obtained from ppRPA based on PBE and B3LYP using the 215-atom supercell and supercell-size extrapolation scheme are presented in Table 2. As shown in Fig. 3, the s-type a_{1g} orbital is within the band gap and three p-type t_{1u} orbitals with higher energies are in the conduction band. Both N-electron and $(N-2)$-electron ground states can be well described by a single KS determinant. We find that TDDFT based on PBE and B3LYP largely underestimates the excitation energy of the $^1T_{1u}$ state by $0.7 \sim 1.6$ eV. As shown

Table 2: VEEs of VO in MgO obtained from the ppRPA approach based on PBE and B3LYP functionals compared with reference values. Supercell-size extrapolated values were obtained from the results of supercells containing 63 and 215 atoms. The geometry of the $^1A_{1g}$ ground state and cc-pVDZ basis set were used. All values are in eV.

Method	$^1T_{1u}$	$^3T_{1u}$
Experiment[98,99]	5.0	2.3∼2.4 (emission)
ppRPA@PBE (supercell 215)	4.89	3.67
ppRPA@PBE (extrapolated)	4.82	3.57
ppRPA@B3LYP (supercell 215)	5.10	3.69
ppRPA@B3LYP (extrapolated)	5.05	3.58
TDDFT@PBE (supercell 215)	3.86	3.29
TDDFT@PBE (extrapolated)	3.37	3.08
TDDFT@B3LYP (supercell 215)	4.60	3.57
TDDFT@B3LYP (extrapolated)	4.29	3.42
BSE/G_0W_0@LDA[100]		3.40
CCSD[42]	5.31	
CCSD[25]	5.28	3.66
CASPT2[101]	5.44	4.09
CAS-DMET[38]	6.26	2.74
NEVPT2-DMET[38]	5.24	2.89
embedded-BSE@DDH[102]	5.23	2.93
FN-DMC[103]		3.80

in Ref. 17, functionals with a higher percentage of the HF exchange are needed for TDDFT to yield improved results. In addition to large underestimations, TDDFT shows an undesired starting-point dependence for VO in MgO, where the difference in VEEs of the $^1T_{1u}$ state from PBE vs. B3LYP is 0.9 eV. Embedding approaches, including regional embedding with the EOM-CCSD solver, NEVPT2-DMET, and embedded BSE@DDH, provide significantly improved accuracy over TDDFT based on conventional functionals, which slightly overestimate the VEE of the $^1T_{1u}$ state by $0.2 \sim 0.3$ eV.

Our ppRPA approach based on both PBE and B3LYP achieves excellent performance. The error of ppRPA@B3LYP for predicting the VEE of the $^1T_{1u}$ state is only 0.05 eV compared with the experiment value. In addition, ppRPA has a weaker DFT starting-point

dependence than TDDFT. The difference between VEEs of the $^1T_{1u}$ state obtained from ppRPA@PBE and ppRPA@B3LYP is only around 0.2 eV, much smaller than the 0.9 eV difference between TDDFT@PBE and TDDFT@B3LYP.

For the VEE of the $^3T_{1u}$ state, all methods in Table 2 overestimate compared with the experimental value since the experimental measurement was conducted for the emission process. As suggested in Ref. 17, an estimation of the Franck-Condon shift is needed for a direct comparison with the emission peak. Nevertheless, comparing to higher-level theories, our ppRPA predictions of the $^3T_{1u}$ VEE are less than 0.1 eV different from CCSD[42] and around 0.2 eV different from fixed-node DMC (FN-DMC).[103] Also, the functional dependence in ppRPA (PBE vs. B3LYP) is only 0.02 eV for the $^3T_{1u}$ state.

4.2.3 C_BC_N in h-BN

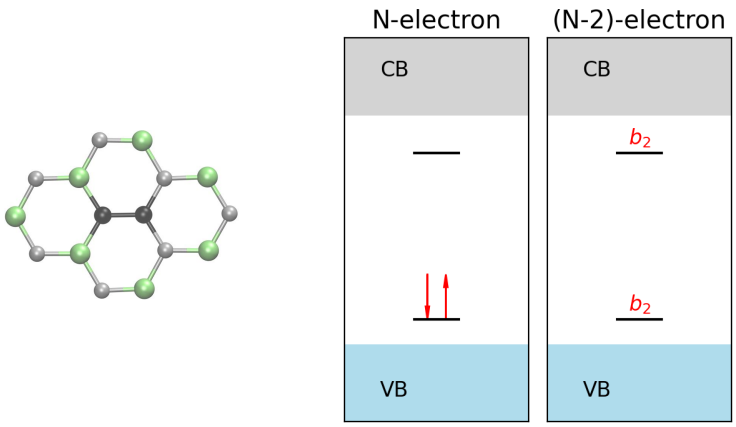

Figure 4: Illustration of defect energy levels and ground-state electron configurations of C_BC_N in h-BN (energy levels are qualitative only).

Our final tested system is C_BC_N in two-dimensional h-BN shown in Fig. 4. The VEEs of the $^1A_1$ state of C_BC_N in h-BN obtained from the ppRPA* approach based on PBE and B3LYP using the 128-atom supercell are presented in Table 3. Due to the difficulty in the SCF convergence of the corresponding $(N-2)$-electron system of C_BC_N in h-BN, KS orbitals and orbital energies from the N-electron system are used in ppRPA* calculations. As shown in Ref. 42, converged excitation energies of C_BC_N in h-BN can be obtained using the 128-

Table 3: VEEs of C_BC_N in h-BN obtained from the ppRPA* approach based on PBE and B3LYP functionals compared with reference values. The geometry of the $^1A_1$ ground state and cc-pVDZ basis set were used. All values are in eV.

Method	$^1A_1$
Experiment[104] [a]	4.6
ppRPA*@PBE (supercell 128)	3.78
ppRPA*@B3LYP (supercell 128)	4.54
TDDFT@PBE (supercell 128)	4.03
TDDFT@B3LYP (supercell 128)	4.63
TDDFT@CAM-B3LYP[105]	4.78
TDDFT@PBE0[104]	4.61
BSE/evGW@PBE0[104]	4.64
ΔSCF@HSE($\alpha = 0.40$)[14] [b]	4.53
CCSD[42]	4.76
cRPA@PBE[40] [b]	3.98
cRPA@HSE[40] [b]	4.23

[a] Estimated vertical excitation energy for C_BC_N in two-dimensional h-BN.
[b] Calculations were performed for C_BC_N in bulk-layered h-BN.

atom supercell model. TDDFT based on hybrid functionals gives VEE errors smaller than 0.2 eV, which are comparable to the results of BSE/evGW@PBE0 and EOM-CCSD. The slightly larger errors in cRPA-based methods may stem from the quality of the approximated dynamical correlation and the use of three-dimensional h-BN structure.[42] ppRPA*@PBE severely underestimates the VEE by 0.8 eV, which is similar to the result of TDDFT@PBE. We suspect the poor performance of ppRPA*@PBE is due to the use of unrelaxed KS orbitals in the non-optimized $(N-2)$-electron ground state. ppRPA* based on B3LYP provides significantly improved accuracy with a VEE error smaller than 0.1 eV. As shown in the SI, the VEE of C_BC_N in h-BN obtained from ppRPA* also converges rapidly with respect to the size of the active space. However, ppRPA* also has a large starting point dependence for calculating excitation energies of VC in diamond with (D_{2d}) geometry (see SI). In addition, for defect systems (e.g., VO in MgO) that have bulk conduction bands or valence bands within defect levels, ppRPA* may misalign states of the N-electron system and fail to predict

excitation energies. This undesired functional dependence and state misalignment issue in ppRPA* suggest the importance of orbital optimization in the $(N-2)$-electron DFT ground state.

4.3 Analysis of Multireference Character

Table 4: NTO weights and associated electron configurations of different defect states obtained from ppRPA@B3LYP. NTO weights larger than 0.05 are shown. NTOs from the hole-hole channel were used in the analysis for NV^- in diamond, SiV^0 in diamond and VV^0 in 4H-SiC. NTOs from the particle-particle channel were used in the analysis for VO in MgO and VC in diamond.

System	State	NTO weight
NV^- in diamond	$^3A_2$	0.990 $\|a_1\bar{a}_1e_xe_y\rangle$
	$^1A_1$	0.424 $\|a_1\bar{a}_1e_x\bar{e}_x\rangle$, 0.423 $\|a_1\bar{a}_1e_y\bar{e}_y\rangle$, 0.152 $\|e_x\bar{e}_xe_y\bar{e}_y\rangle$
SiV^0 in diamond	$^3A_{2g}$	0.906 $\|e_{ux}\bar{e}_{ux}e_{uy}\bar{e}_{uy}e_{gx}e_{gy}\rangle$
	$^3A_{2u}$	0.475 $\|e_{ux}\bar{e}_{ux}e_{uy}e_{gx}e_{gy}\bar{e}_{gy}\rangle$, 0.475 $\|e_{ux}e_{uy}\bar{e}_{uy}e_{gx}\bar{e}_{gx}e_{gy}\rangle$
	$^3A_{1u}$	0.467 $\|e_{ux}\bar{e}_{ux}e_{uy}e_{gx}\bar{e}_{gx}e_{gy}\rangle$, 0.467 $\|e_{ux}e_{uy}\bar{e}_{uy}e_{gx}e_{gy}\bar{e}_{gy}\rangle$
VV^0 in 4H-SiC	$^3A_2$	0.973 $\|a_1\bar{a}_1e_xe_y\rangle$
	$^1A_1$	0.443 $\|a_1\bar{a}_1e_x\bar{e}_x\rangle$, 0.442 $\|a_1\bar{a}_1e_y\bar{e}_y\rangle$, 0.114 $\|e_x\bar{e}_xe_y\bar{e}_y\rangle$
VO in MgO	$^1A_{1g}$	0.982 $\|a_{1g}\bar{a}_{1g}\rangle$
VC in diamond (D_{2d})	$^1A_1$	0.875 $\|b_2\bar{b}_2\rangle$, 0.067 $\|e_x\bar{e}_x\rangle$, 0.067 $\|e_y\bar{e}_y\rangle$

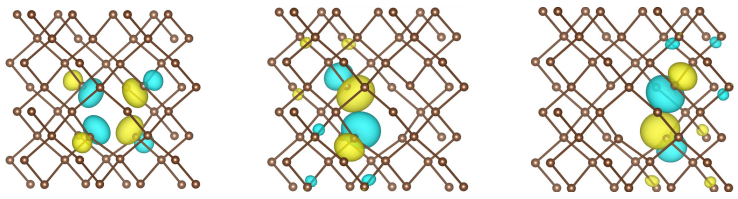

Figure 5: Dominant two-electron addition NTOs of the $^1A_1$ ground state of VC in diamond (D_{2d}) obtained from ppRPA@B3LYP calculation of the 63-atom supercell. Isosurface value is 0.08 a.u. NTO weights are 0.875 (left), 0.067 (middle), and 0.067 (right).

In this section, we further analyze the character of defect ground and excited states using the NTO approach in ppRPA on systems studied in this and previous works.[72] NTO weights and associated electron configurations of different defect states obtained from ppRPA@B3LYP are tabulated in Table 4. For NV^- in diamond, only one dominant NTO weight of 0.990

can be found in the $^3A_2$ ground state, which means it can be properly described by a single-determinant method. For the $^1A_1$ state, two approximately equivalent NTO weights corresponding to two singly-excited electron configurations indicate a strong multireference character. The doubly-excited configuration $|e_x\bar{e}_x e_y\bar{e}_y\rangle$ with a NTO weight of 0.152 is also found in the $^1A_1$ state, which agrees with the analysis using QDET in Ref. 18. Similar observations are found for VV^0 in 4H-SiC, where the $^3A_2$ ground state is dominant with a single determinant, and the $^1A_1$ state has a strong multireference character. For SiV^0 in diamond, the $^3A_{2g}$ ground state shows a dominant NTO weight of 0.906, while two excited states ($^3A_{2u}$ and $^3A_{1u}$) show strong multireference characters. The dominant NTO weight of 0.982 can be found in the $^1A_{1g}$ ground state of VO in MgO, which explains the good accuracy of single-reference methods in Table 2. For VC in diamond of the D_{2d} symmetry, the multireference character is found in the $^1A_1$ ground state. In addition to the 87% contribution from the $|b_2\bar{b}_2\rangle$ configuration, the singlet ground state has 13% contribution from doubly-excited configurations $|e_x\bar{e}_x\rangle$ and $|e_y\bar{e}_y\rangle$, which cannot be captured by the single-determinant KS-DFT approach. This analysis agrees with the unsatisfactory accuracy of TDDFT in Table 1.

Furthermore, in Fig. 5, we plot the dominant two-electron addition NTOs of the $^1A_1$ ground state of VC in diamond (D_{2d} geometry) obtained from ppRPA@B3LYP. The electron configurations of this state can be approximately described by three doubly-occupied NTOs as 87.5% contribution from $|b_2\bar{b}_2\rangle$, 6.7% contribution from $|e_x\bar{e}_x\rangle$ and 6.7% contribution from $|e_y\bar{e}_y\rangle$. These NTOs show that the two valence electrons are relatively localized around the carbon vacancy center.

4.4 Comparison between Two Channels in ppRPA

In this paper and our previous work,[72] we have shown that both the particle-particle and hole-hole channels in ppRPA can be used to calculate excitation energies of point defects. In practice, the choice of the channel depends on the electron configuration of defect systems. By starting from an appropriate reference system, all desired defect ground and excited

states should be accessible from two-electron additions in the particle-particle channel or two-electron removals in the hole-hole channel.

For example, NV^- in diamond has four occupied and two virtual spin-orbitals as the defect levels. By starting with the $(N+2)$-electron reference system that adds two electrons to $\bar{e}_x$ and $\bar{e}_y$ orbitals, all relevant defect states can be obtained by removing two electrons in different combinations of two spin-orbitals. In addition, the $(N+2)$-electron state of NV^- in diamond is closed-shell, which can be well described by the single-reference KS-DFT formalism. However, if starting with the $(N-2)$-electron system that removes two electrons from e_x and e_y orbitals, several defect states that excite electrons from orbitals below HOMO (e.g., ^{3}E) cannot be obtained. Therefore, the hole-hole channel starting with $(N+2)$-electron system is chosen for NV^- in diamond and defect systems with similar electron configurations.[72]

Similarly, VC in diamond with D_{2d} symmetry has two occupied and four virtual spin-orbitals as the defect levels. By starting with the closed-shell $(N-2)$-electron reference system that removes two electrons to b_2 and $\bar{b}_2$ orbitals, all relevant defect states can be obtained by adding two electrons in different combinations of two spin-orbitals. However, if starting with the $(N+2)$-electron system that adds two electrons from e_x and e_y orbitals, several defect states that excite two electrons from b_2 and $\bar{b}_2$ orbitals (e.g., A_1, B_1 and B_2) cannot be obtained. Moreover, the ground state of the $(N+2)$-electron system is triplet, which can be challenging for the KS-DFT formalism to describe accurately. Therefore, the particle-particle channel starting with $(N-2)$-electron system is chosen for VC in diamond with D_{2d} symmetry and other defect systems in this work.

5 CONCLUSIONS

In summary, we applied the ppRPA approach within the particle-particle channel to predict accurate excitation energies of point defect systems in this work. In ppRPA simulations, the

ground-state SCF calculation for $(N-2)$-electron system is first performed, then excitation energies are obtained as the differences between two-electron addition energies. To reduce the computational cost, the ppRPA equation is solved with the Davidson algorithm in an active space consisting of canonical orbitals, followed by an extrapolation scheme to obtain the full-space results. We demonstrated that ppRPA provides a balanced description of correlated excited states in all tested defect systems, including VC in diamond, VO in MgO, and C_BC_N in h-BN. The errors from ppRPA@B3LYP for predicting vertical excitation energies of the tested point defects are mostly smaller than 0.1 eV. In particular, ppRPA achieves good accuracy for excitation energies of VC in diamond with various geometries, which is challenging for single-reference methods. This good performance is a result of seamless Fock space embedding in ppRPA, which captures explicitly the correlated interactions of two particles or two holes in the medium of the N-electron system described with a density functional approximation.[51] Furthermore, we developed the NTO approach in ppRPA, which provides important physical insights into electronic transitions in defect systems and the multireference character of associated states. We conclude that ppRPA shows promise as a low-cost yet accurate tool for investigating excited-state properties of point defect systems.

Acknowledgement

T.Z. and J.L. are supported by the National Science Foundation (Grant No. CHE-2337991) and a start-up fund from Yale University. J.L. also acknowledges support from the Tony Massini Postdoctoral Fellowship in Data Science. Y.J. acknowledges support from the Midwest Integrated Center for Computational Materials (MICCoM) as part of the Computational Materials Science Program funded by the U.S. Department of Energy, Office of Science, Office of Basic Energy Sciences, under Contract No. DE-AC02-06CH11357. J.Y. and W.Y. acknowledge the support from the National Science Foundation (Grant No. CHE-2154831).

Supporting Information

Details about geometry optimizations, tabulated excitation energies of defects obtained from ppRPA, basis set convergence in ppRPA, tabulated excitation energies of defects obtained from TDDFT, ppRPA* results for VC in diamond and VO in MgO.

Data Availability Statement

The data that support the findings of this study are available in the main text and the supporting information.

References

(1) Dreyer, C. E.; Alkauskas, A.; Lyons, J. L.; Janotti, A.; Van de Walle, C. G. First-Principles Calculations of Point Defects for Quantum Technologies. *Annu. Rev. Mater. Res.* **2018**, *48*, 1–26.

(2) Wolfowicz, G.; Heremans, F. J.; Anderson, C. P.; Kanai, S.; Seo, H.; Gali, A.; Galli, G.; Awschalom, D. D. Quantum Guidelines for Solid-State Spin Defects. *Nat. Rev. Mater.* **2021**, *6*, 906–925.

(3) Jelezko, F.; Gaebel, T.; Popa, I.; Domhan, M.; Gruber, A.; Wrachtrup, J. Observation of Coherent Oscillation of a Single Nuclear Spin and Realization of a Two-Qubit Conditional Quantum Gate. *Phys. Rev. Lett.* **2004**, *93*, 130501.

(4) Weber, J. R.; Koehl, W. F.; Varley, J. B.; Janotti, A.; Buckley, B. B.; Van de Walle, C. G.; Awschalom, D. D. Quantum Computing with Defects. *Proc. Natl. Acad. Sci.* **2010**, *107*, 8513–8518.

(5) Anderson, C. P.; Glen, E. O.; Zeledon, C.; Bourassa, A.; Jin, Y.; Zhu, Y.; Vorwerk, C.; Crook, A. L.; Abe, H.; Ul-Hassan, J.; Ohshima, T.; Son, N. T.; Galli, G.;

Awschalom, D. D. Five-Second Coherence of a Single Spin with Single-Shot Readout in Silicon Carbide. *Sci. Adv.* **2022**, *8*, eabm5912.

(6) Childress, L.; Gurudev Dutt, M. V.; Taylor, J. M.; Zibrov, A. S.; Jelezko, F.; Wrachtrup, J.; Hemmer, P. R.; Lukin, M. D. Coherent Dynamics of Coupled Electron and Nuclear Spin Qubits in Diamond. *Science* **2006**, *314*, 281–285.

(7) Gali, Á. Ab Initio Theory of the Nitrogen-Vacancy Center in Diamond. *Nanophotonics* **2019**, *8*, 1907–1943.

(8) Hohenberg, P.; Kohn, W. Inhomogeneous Electron Gas. *Phys. Rev.* **1964**, *136*, B864–B871.

(9) Kohn, W.; Sham, L. J. Self-Consistent Equations Including Exchange and Correlation Effects. *Phys. Rev.* **1965**, *140*, A1133–A1138.

(10) Parr, R. G.; Weitao, Y. *Density-Functional Theory of Atoms and Molecules*; Oxford University Press, 1989.

(11) Casida, M. E. *Recent Advances in Density Functional Methods*; Recent Advances in Computational Chemistry; WORLD SCIENTIFIC, 1995; Vol. Volume 1; pp 155–192.

(12) Ullrich, C. A. *Time-Dependent Density-Functional Theory: Concepts and Applications*; OUP Oxford, 2011.

(13) Zwijnenburg, M. A.; Sousa, C.; Sokol, A. A.; Bromley, S. T. Optical Excitations of Defects in Realistic Nanoscale Silica Clusters: Comparing the Performance of Density Functional Theory Using Hybrid Functionals with Correlated Wavefunction Methods. *J. Chem. Phys.* **2008**, *129*, 014706.

(14) Mackoit-Sinkevičienė, M.; Maciaszek, M.; Van de Walle, C. G.; Alkauskas, A. Carbon Dimer Defect as a Source of the 4.1 eV Luminescence in Hexagonal Boron Nitride. *Appl. Phys. Lett.* **2019**, *115*, 212101.

(15) Jin, Y.; Govoni, M.; Wolfowicz, G.; Sullivan, S. E.; Heremans, F. J.; Awschalom, D. D.; Galli, G. Photoluminescence Spectra of Point Defects in Semiconductors: Validation of First-Principles Calculations. *Phys. Rev. Mater.* **2021**, *5*, 084603.

(16) Mackrodt, W. C.; Gentile, F. S.; Dovesi, R. The Calculated Energies and Charge and Spin Distributions of the Excited GR1 State in Diamond. *J. Chem. Phys.* **2022**, *156*, 044708.

(17) Jin, Y.; Yu, V. W.-z.; Govoni, M.; Xu, A. C.; Galli, G. Excited State Properties of Point Defects in Semiconductors and Insulators Investigated with Time-Dependent Density Functional Theory. *J. Chem. Theory Comput.* **2023**, *19*, 8689–8705.

(18) Jin, Y.; Govoni, M.; Galli, G. Vibrationally Resolved Optical Excitations of the Nitrogen-Vacancy Center in Diamond. *npj Comput. Mater.* **2022**, *8*, 1–9.

(19) Cohen, A. J.; Mori-Sánchez, P.; Yang, W. Challenges for Density Functional Theory. *Chem. Rev.* **2012**, *112*, 289–320.

(20) Zhu, T.; de Silva, P.; van Aggelen, H.; Van Voorhis, T. Many-Electron Expansion: A Density Functional Hierarchy for Strongly Correlated Systems. *Phys. Rev. B* **2016**, *93*, 201108.

(21) Zhu, T.; de Silva, P.; Van Voorhis, T. Implementation of the Many-Pair Expansion for Systematically Improving Density Functional Calculations of Molecules. *J. Chem. Theory Comput.* **2019**, *15*, 1089–1101.

(22) Salpeter, E. E.; Bethe, H. A. A Relativistic Equation for Bound-State Problems. *Phys. Rev.* **1951**, *84*, 1232–1242.

(23) Sham, L. J.; Rice, T. M. Many-Particle Derivation of the Effective-Mass Equation for the Wannier Exciton. *Phys. Rev.* **1966**, *144*, 708–714.

(24) Hanke, W.; Sham, L. J. Many-Particle Effects in the Optical Excitations of a Semiconductor. *Phys. Rev. Lett.* **1979**, *43*, 387–390.

(25) Gallo, A.; Hummel, F.; Irmler, A.; Grüneis, A. A Periodic Equation-of-Motion Coupled-Cluster Implementation Applied to F-centers in Alkaline Earth Oxides. *J. Chem. Phys.* **2021**, *154*, 064106.

(26) Simula, K. A.; Makkonen, I. Calculation of the Energies of the Multideterminant States of the Nitrogen Vacancy Center in Diamond with Quantum Monte Carlo. *Phys. Rev. B* **2023**, *108*, 094108.

(27) Sun, Q.; Chan, G. K.-L. Quantum Embedding Theories. *Acc. Chem. Res.* **2016**, *49*, 2705–2712.

(28) Cui, Z.-H.; Zhu, T.; Chan, G. K.-L. Efficient Implementation of Ab Initio Quantum Embedding in Periodic Systems: Density Matrix Embedding Theory. *J. Chem. Theory Comput.* **2020**, *16*, 119–129.

(29) Zhu, T.; Cui, Z.-H.; Chan, G. K.-L. Efficient Formulation of Ab Initio Quantum Embedding in Periodic Systems: Dynamical Mean-Field Theory. *J. Chem. Theory Comput.* **2020**, *16*, 141–153.

(30) Zhu, T.; Chan, G. K.-L. Ab Initio Full Cell GW+DMFT for Correlated Materials. *Phys. Rev. X* **2021**, *11*, 021006.

(31) Zhu, T.; Peng, L.; Zhai, H.; Cui, Z.-H.; Chan, G. K.-L. Towards an exact electronic quantum many-body treatment of Kondo correlation in magnetic impurities. *arXiv preprint arXiv:2405.18709* **2024**,

(32) Li, J.; Zhu, T. Interacting-bath dynamical embedding for capturing non-local electron correlation in solids. *arXiv preprint arXiv:2406.07531* **2024**,

(33) Ma, H.; Govoni, M.; Galli, G. Quantum Simulations of Materials on Near-Term Quantum Computers. *npj Comput. Mater.* **2020**, *6*, 1–8.

(34) Ma, H.; Sheng, N.; Govoni, M.; Galli, G. Quantum Embedding Theory for Strongly Correlated States in Materials. *J. Chem. Theory Comput.* **2021**, *17*, 2116–2125.

(35) Sheng, N.; Vorwerk, C.; Govoni, M.; Galli, G. Green's Function Formulation of Quantum Defect Embedding Theory. *J. Chem. Theory Comput.* **2022**, *18*, 3512–3522.

(36) Mitra, A.; Pham, H. Q.; Pandharkar, R.; Hermes, M. R.; Gagliardi, L. Excited States of Crystalline Point Defects with Multireference Density Matrix Embedding Theory. *J. Phys. Chem. Lett.* **2021**, *12*, 11688–11694.

(37) Haldar, S.; Mitra, A.; Hermes, M. R.; Gagliardi, L. Local Excitations of a Charged Nitrogen Vacancy in Diamond with Multireference Density Matrix Embedding Theory. *J. Phys. Chem. Lett.* **2023**, *14*, 4273–4280.

(38) Verma, S.; Mitra, A.; Jin, Y.; Haldar, S.; Vorwerk, C.; Hermes, M. R.; Galli, G.; Gagliardi, L. Optical Properties of Neutral F Centers in Bulk MgO with Density Matrix Embedding. *J. Phys. Chem. Lett.* **2023**, *14*, 7703–7710.

(39) Bockstedte, M.; Schütz, F.; Garratt, T.; Ivády, V.; Gali, A. Ab Initio Description of Highly Correlated States in Defects for Realizing Quantum Bits. *npj Quantum Mater.* **2018**, *3*, 1–6.

(40) Muechler, L.; Badrtdinov, D. I.; Hampel, A.; Cano, J.; Rösner, M.; Dreyer, C. E. Quantum Embedding Methods for Correlated Excited States of Point Defects: Case Studies and Challenges. *Phys. Rev. B* **2022**, *105*, 235104.

(41) Romanova, M.; Weng, G.; Apelian, A.; Vlček, V. Dynamical Downfolding for Localized Quantum States. *npj Comput. Mater.* **2023**, *9*, 1–9.

(42) Lau, B. T. G.; Busemeyer, B.; Berkelbach, T. C. Optical Properties of Defects in Solids via Quantum Embedding with Good Active Space Orbitals. *J. Phys. Chem. C* **2024**, *128*, 2959–2966.

(43) van Aggelen, H.; Yang, Y.; Yang, W. Exchange-Correlation Energy from Pairing Matrix Fluctuation and the Particle-Particle Random-Phase Approximation. *Phys. Rev. A* **2013**, *88*, 030501.

(44) van Aggelen, H.; Yang, Y.; Yang, W. Exchange-Correlation Energy from Pairing Matrix Fluctuation and the Particle-Particle Random Phase Approximation. *J. Chem. Phys.* **2014**, *140*, 18A511.

(45) Ring, P.; Schuck, P. *The Nuclear Many-Body Problem*, softcover repri edition ed.; Springer: Berlin Heidelberg, 2004.

(46) Ripka, S. R. P. G.; Blaizot, J.-P.; Ripka, G. *Quantum Theory of Finite Systems*; MIT Press, 1986.

(47) Yang, Y.; van Aggelen, H.; Steinmann, S. N.; Peng, D.; Yang, W. Benchmark Tests and Spin Adaptation for the Particle-Particle Random Phase Approximation. *J. Chem. Phys.* **2013**, *139*, 174110.

(48) Yang, Y.; van Aggelen, H.; Yang, W. Double, Rydberg and Charge Transfer Excitations from Pairing Matrix Fluctuation and Particle-Particle Random Phase Approximation. *J. Chem. Phys.* **2013**, *139*, 224105.

(49) Yang, Y.; Peng, D.; Lu, J.; Yang, W. Excitation Energies from Particle-Particle Random Phase Approximation: Davidson Algorithm and Benchmark Studies. *J. Chem. Phys.* **2014**, *141*, 124104.

(50) Yang, Y.; Peng, D.; Davidson, E. R.; Yang, W. Singlet–Triplet Energy Gaps for Dirad-

icals from Particle–Particle Random Phase Approximation. *J. Phys. Chem. A* **2015**, *119*, 4923–4932.

(51) Zhang, D.; Yang, W. Accurate and Efficient Calculation of Excitation Energies with the Active-Space Particle-Particle Random Phase Approximation. *J. Chem. Phys.* **2016**, *145*, 144105.

(52) Yang, Y.; Dominguez, A.; Zhang, D.; Lutsker, V.; Niehaus, T. A.; Frauenheim, T.; Yang, W. Charge Transfer Excitations from Particle-Particle Random Phase Approximation—Opportunities and Challenges Arising from Two-Electron Deficient Systems. *J. Chem. Phys.* **2017**, *146*, 124104.

(53) Chen, Z.; Zhang, D.; Jin, Y.; Yang, Y.; Su, N. Q.; Yang, W. Multireference Density Functional Theory with Generalized Auxiliary Systems for Ground and Excited States. *J. Phys. Chem. Lett.* **2017**, *8*, 4479–4485.

(54) Pinter, B.; Al-Saadon, R.; Chen, Z.; Yang, W. Spin-State Energetics of Iron(II) Porphyrin from the Particle-Particle Random Phase Approximation. *Eur. Phys. J. B* **2018**, *91*, 270.

(55) Al-Saadon, R.; Sutton, C.; Yang, W. Accurate Treatment of Charge-Transfer Excitations and Thermally Activated Delayed Fluorescence Using the Particle–Particle Random Phase Approximation. *J. Chem. Theory Comput.* **2018**, *14*, 3196–3204.

(56) Li, J.; Chen, Z.; Yang, W. Multireference Density Functional Theory for Describing Ground and Excited States with Renormalized Singles. *J. Phys. Chem. Lett.* **2022**, *13*, 894–903.

(57) Bannwarth, C.; Yu, J. K.; Hohenstein, E. G.; Martínez, T. J. Hole–Hole Tamm–Dancoff-approximated Density Functional Theory: A Highly Efficient Electronic Structure Method Incorporating Dynamic and Static Correlation. *J. Chem. Phys.* **2020**, *153*, 024110.

(58) Yu, J. K.; Bannwarth, C.; Hohenstein, E. G.; Martínez, T. J. Ab Initio Nonadiabatic Molecular Dynamics with Hole–Hole Tamm–Dancoff Approximated Density Functional Theory. *J. Chem. Theory Comput.* **2020**, *16*, 5499–5511.

(59) Hohenstein, E. G.; Yu, J. K.; Bannwarth, C.; List, N. H.; Paul, A. C.; Folkestad, S. D.; Koch, H.; Martínez, T. J. Predictions of Pre-edge Features in Time-Resolved Near-Edge X-ray Absorption Fine Structure Spectroscopy from Hole–Hole Tamm–Dancoff-Approximated Density Functional Theory. *J. Chem. Theory Comput.* **2021**, *17*, 7120–7133.

(60) Yang, Y.; Shen, L.; Zhang, D.; Yang, W. Conical Intersections from Particle–Particle Random Phase and Tamm–Dancoff Approximations. *J. Phys. Chem. Lett.* **2016**, *7*, 2407–2411.

(61) Zhang, D.; Peng, D.; Zhang, P.; Yang, W. Analytic Gradients, Geometry Optimization and Excited State Potential Energy Surfaces from the Particle-Particle Random Phase Approximation. *Phys. Chem. Chem. Phys.* **2014**, *17*, 1025–1038.

(62) Peng, D.; Steinmann, S. N.; van Aggelen, H.; Yang, W. Equivalence of Particle-Particle Random Phase Approximation Correlation Energy and Ladder-Coupled-Cluster Doubles. *J. Chem. Phys.* **2013**, *139*, 104112.

(63) Scuseria, G. E.; Henderson, T. M.; Bulik, I. W. Particle-Particle and Quasiparticle Random Phase Approximations: Connections to Coupled Cluster Theory. *J. Chem. Phys.* **2013**, *139*, 104113.

(64) Berkelbach, T. C. Communication: Random-phase Approximation Excitation Energies from Approximate Equation-of-Motion Coupled-Cluster Doubles. *J. Chem. Phys.* **2018**, *149*, 041103.

(65) Zhang, D.; Su, N. Q.; Yang, W. Accurate Quasiparticle Spectra from the T-Matrix

Self-Energy and the Particle–Particle Random Phase Approximation. *J. Phys. Chem. Lett.* **2017**, *8*, 3223–3227.

(66) Li, J.; Chen, Z.; Yang, W. Renormalized Singles Green's Function in the T-Matrix Approximation for Accurate Quasiparticle Energy Calculation. *J. Phys. Chem. Lett.* **2021**, *12*, 6203–6210.

(67) Orlando, R.; Romaniello, P.; Loos, P.-F. The Three Channels of Many-Body Perturbation Theory: GW, Particle–Particle, and Electron–Hole T-matrix Self-Energies. *J. Chem. Phys.* **2023**, *159*, 184113.

(68) Li, J.; Yu, J.; Chen, Z.; Yang, W. Linear Scaling Calculations of Excitation Energies with Active-Space Particle–Particle Random-Phase Approximation. *J. Phys. Chem. A* **2023**, *127*, 7811–7822.

(69) Loos, P.-F.; Romaniello, P. Static and Dynamic Bethe–Salpeter Equations in the T-matrix Approximation. *J. Chem. Phys.* **2022**, *156*, 164101.

(70) Orlando, R.; Romaniello, P.; Loos, P.-F. In *Advances in Quantum Chemistry*; Hoggan, P. E., Ed.; Academic Press, 2023; Vol. 88; pp 183–211.

(71) Monino, E.; Loos, P.-F. Connections and Performances of Green's Function Methods for Charged and Neutral Excitations. *J. Chem. Phys.* **2023**, *159*, 034105.

(72) Li, J.; Jin, Y.; Yu, J.; Yang, W.; Zhu, T. Accurate Excitation Energies of Point Defects from Fast Particle–Particle Random Phase Approximation Calculations. *J. Phys. Chem. Lett.* **2024**, *15*, 2757–2764.

(73) Becke, A. D. Density-functional Thermochemistry. III. The Role of Exact Exchange. *J. Chem. Phys.* **1993**, *98*, 5648–5652.

(74) Lee, C.; Yang, W.; Parr, R. G. Development of the Colle-Salvetti Correlation-Energy Formula into a Functional of the Electron Density. *Phys. Rev. B* **1988**, *37*, 785–789.

(75) Martin, R. L. Natural Transition Orbitals. *J. Chem. Phys.* **2003**, *118*, 4775–4777.

(76) Krause, K.; Klopper, W. Implementation of the Bethe-Salpeter Equation in the TURBOMOLE Program. *J. Comput. Chem.* **2017**, *38*, 383–388.

(77) Cho, Y.; Bintrim, S. J.; Berkelbach, T. C. Simplified GW/BSE Approach for Charged and Neutral Excitation Energies of Large Molecules and Nanomaterials. *J. Chem. Theory Comput.* **2022**, *18*, 3438–3446.

(78) Glendening, E. D.; Landis, C. R.; Weinhold, F. NBO 6.0: Natural Bond Orbital Analysis Program. *J. Comput. Chem.* **2013**, *34*, 1429–1437.

(79) Zhang, J.-X.; Sheong, F. K.; Lin, Z. Unravelling Chemical Interactions with Principal Interacting Orbital Analysis. *Chem. Eur. J.* **2018**, *24*, 9639–9650.

(80) Glendening, E. D.; Weinhold, F. Resonance Natural Bond Orbitals: Efficient Semilocalized Orbitals for Computing and Visualizing Reactive Chemical Processes. *J. Chem. Theory Comput.* **2019**, *15*, 916–921.

(81) Yu, J.; Su, N. Q.; Yang, W. Describing Chemical Reactivity with Frontier Molecular Orbitalets. *JACS Au* **2022**, *2*, 1383–1394.

(82) Long Gu, F.; Yu, J.; Yang, W. *Exploring Chemical Concepts Through Theory and Computation*; John Wiley & Sons, Ltd, 2024; Chapter 1, pp 1–22.

(83) Zhu, T.; de Silva, P.; Van Voorhis, T. Self-attractive Hartree decomposition: Partitioning electron density into smooth localized fragments. *J. Chem. Theory Comput.* **2018**, *14*, 92–103.

(84) ROWE, D. J. Equations-of-Motion Method and the Extended Shell Model. *Rev. Mod. Phys.* **1968**, *40*, 153–166.

(85) Peng, D.; van Aggelen, H.; Yang, Y.; Yang, W. Linear-Response Time-Dependent Density-Functional Theory with Pairing Fields. *J. Chem. Phys.* **2014**, *140*, 18A522.

(86) Perdew, J. P.; Burke, K.; Ernzerhof, M. Generalized Gradient Approximation Made Simple. *Phys. Rev. Lett.* **1996**, *77*, 3865–3868.

(87) Giannozzi, P.; Baseggio, O.; Bonfà, P.; Brunato, D.; Car, R.; Carnimeo, I.; Cavazzoni, C.; de Gironcoli, S.; Delugas, P.; Ferrari Ruffino, F.; Ferretti, A.; Marzari, N.; Timrov, I.; Urru, A.; Baroni, S. Quantum ESPRESSO toward the Exascale. *J. Chem. Phys.* **2020**, *152*, 154105.

(88) Carnimeo, I.; Affinito, F.; Baroni, S.; Baseggio, O.; Bellentani, L.; Bertossa, R.; Delugas, P. D.; Ruffino, F. F.; Orlandini, S.; Spiga, F.; Giannozzi, P. Quantum ESPRESSO: One Further Step toward the Exascale. *J. Chem. Theory Comput.* **2023**, *19*, 6992–7006.

(89) Sun, Q.; Berkelbach, T. C.; Blunt, N. S.; Booth, G. H.; Guo, S.; Li, Z.; Liu, J.; McClain, J. D.; Sayfutyarova, E. R.; Sharma, S.; Wouters, S.; Chan, G. K.-L. PySCF: The Python-based Simulations of Chemistry Framework. *WIREs Comput. Mol. Sci.* **2018**, *8*, e1340.

(90) Sun, Q.; Zhang, X.; Banerjee, S.; Bao, P.; Barbry, M.; Blunt, N. S.; Bogdanov, N. A.; Booth, G. H.; Chen, J.; Cui, Z.-H.; Eriksen, J. J.; Gao, Y.; Guo, S.; Hermann, J.; Hermes, M. R.; Koh, K.; Koval, P.; Lehtola, S.; Li, Z.; Liu, J.; Mardirossian, N.; McClain, J. D.; Motta, M.; Mussard, B.; Pham, H. Q.; Pulkin, A.; Purwanto, W.; Robinson, P. J.; Ronca, E.; Sayfutyarova, E. R.; Scheurer, M.; Schurkus, H. F.; Smith, J. E. T.; Sun, C.; Sun, S.-N.; Upadhyay, S.; Wagner, L. K.; Wang, X.; White, A.; Whitfield, J. D.; Williamson, M. J.; Wouters, S.; Yang, J.; Yu, J. M.; Zhu, T.; Berkelbach, T. C.; Sharma, S.; Sokolov, A. Y.; Chan, G. K.-L. Recent Developments in the PySCF Program Package. *J. Chem. Phys.* **2020**, *153*, 024109.

(91) Dunning, T. H. Gaussian Basis Sets for Use in Correlated Molecular Calculations. I. The Atoms Boron through Neon and Hydrogen. *J. Chem. Phys.* **1989**, *90*, 1007–1023.

(92) Weigend, F.; Köhn, A.; Hättig, C. Efficient Use of the Correlation Consistent Basis Sets in Resolution of the Identity MP2 Calculations. *J. Chem. Phys.* **2002**, *116*, 3175–3183.

(93) Li, J.; Yu, J.; Yang, W. unpublished.

(94) Lannoo, M.; Stoneham, A. M. The Optical Absorption of the Neutral Vacancy in Diamond. *J. Phys. Chem. Solids* **1968**, *29*, 1987–2000.

(95) Hood, R. Q.; Kent, P. R. C.; Needs, R. J.; Briddon, P. R. Quantum Monte Carlo Study of the Optical and Diffusive Properties of the Vacancy Defect in Diamond. *Phys. Rev. Lett.* **2003**, *91*, 076403.

(96) Clark, C. D.; Walker, J.; Ditchburn, R. W. The Neutral Vacancy in Diamond. *Proceedings of the Royal Society of London. A. Mathematical and Physical Sciences* **1997**, *334*, 241–257.

(97) Davies, G. The Jahn-Teller Effect and Vibronic Coupling at Deep Levels in Diamond. *Rep. Prog. Phys.* **1981**, *44*, 787.

(98) Chen, Y.; Williams, R. T.; Sibley, W. A. Defect Cluster Centers in MgO. *Phys. Rev.* **1969**, *182*, 960–964.

(99) Kappers, L. A.; Kroes, R. L.; Hensley, E. B. F^+ and F' Centers in Magnesium Oxide. *Phys. Rev. B* **1970**, *1*, 4151–4157.

(100) Rinke, P.; Schleife, A.; Kioupakis, E.; Janotti, A.; Rödl, C.; Bechstedt, F.; Scheffler, M.; Van de Walle, C. G. First-Principles Optical Spectra for F Centers in MgO. *Phys. Rev. Lett.* **2012**, *108*, 126404.

(101) Sousa, C.; Illas, F. On the Accurate Prediction of the Optical Absorption Energy of F-centers in MgO from Explicitly Correlated Ab Initio Cluster Model Calculations. *J. Chem. Phys.* **2001**, *115*, 1435–1439.

(102) Vorwerk, C.; Galli, G. Disentangling Photoexcitation and Photoluminescence Processes in Defective MgO. *Phys. Rev. Mater.* **2023**, *7*, 033801.

(103) Ertekin, E.; Wagner, L. K.; Grossman, J. C. Point-Defect Optical Transitions and Thermal Ionization Energies from Quantum Monte Carlo Methods: Application to the F-Center Defect in MgO. *Phys. Rev. B* **2013**, *87*, 155210.

(104) Winter, M.; Bousquet, M. H. E.; Jacquemin, D.; Duchemin, I.; Blase, X. Photoluminescent Properties of the Carbon-Dimer Defect in Hexagonal Boron-Nitride: A Many-Body Finite-Size Cluster Approach. *Phys. Rev. Mater.* **2021**, *5*, 095201.

(105) Korona, T.; Chojecki, M. Exploring Point Defects in Hexagonal Boron-Nitrogen Monolayers. *Int. J. Quantum Chem.* **2019**, *119*, e25925.

TOC Graphic

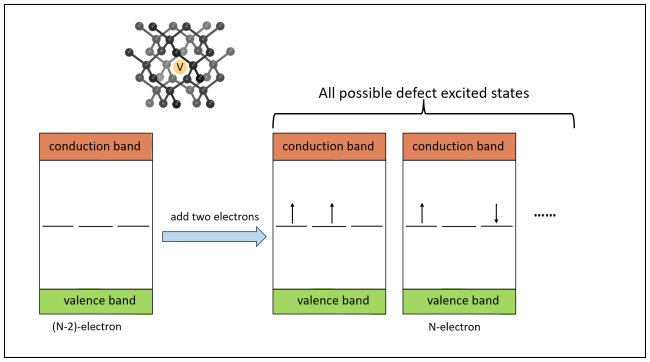
V
All possible defect excited states
conduction band
valence band
(N-2)-electron
add two electrons
conduction band
valence band
conduction band
valence band
N-electron